Critical behaviors of melting and high-temperature structures in stage-1 rubidium-graphite intercalation compounds

Naoto Metoki and Hiroyoshi Suematsu
Department of Physics, Faculty of Science, University of Tokyo, Bunkyo-ku, Tokyo 113, Japan
(Received 17 December 1987)

The phase diagram, the high-temperature (T) structures of liquid and solids, and the critical behaviors of melting in stage-1 Rb-graphite intercalation compounds have been investigated with use of x-ray diffraction. The (P_{Rb}, T) phase diagram shows a narrow region of a high-T $\alpha\beta$ stacking solid with the in-plane (2×2) structure between the low-T $\alpha\beta\gamma\delta$ solid and the high-T liquid. At high temperatures Rb atoms behave as a quasi-two-dimensional liquid with in-plane correlations, and as T approaches T_m (melting temperature) they have strong in-plane and out-of-plane correlations with the same symmetry as the $\alpha\beta$ solid; the two-dimensional (2D) to 3D crossover effect is observed. Remarkable features of the continuous melting are observed at T_m: (1) the peak wave number of the in-plane short-range order in the liquid changes continuously to the Bragg peak wave number of the $\alpha\beta$ solid, (2) the order parameter of the $\alpha\beta$ solid grows continuously with $\beta=0.30\pm0.06$, and (3) the in-plane positional and orientational correlation lengths ξ increase in the *solid* and the liquid and have critical exponents $\nu_a=0.24\pm0.04$ and $\nu_\phi=0.34\pm0.04$ in the liquid, respectively. All the critical parameters show no appreciable hysteresis at T_m. Contrary to these continuous behaviors, the correlation lengths remain finite at T_m, suggesting the presence of a small but finite first-order gap. These experimental results are discussed in terms of the 3D four-state Potts model. In the low-P_{Rb} case, the transition is of first order in contrast to the high-P_{Rb} case mentioned above. In some samples, the maximum temperature in $\xi(T)$ which is obtained in the off-Bragg scan shifts a few degrees lower than T_m. Some discussions are given. The $\alpha\beta$ solid at high T shows remarkable in-plane anisotropic Debye-Waller factors.

I. INTRODUCTION

Graphite intercalation compounds[1-3] (GIC's) exhibit various types of structural phase transitions, such as staging,[4-8] in-plane ordering[9,10] of intercalant atoms and stacking ordering[11] of both graphite and intercalant layers. Intercalant layers form a two-dimensional (2D) ordering commensurate or incommensurate with graphite lattice at low temperatures, and at elevated temperatures they melt into a quasi-2D liquid in which the migration of intercalant atoms is restricted in the 2D gallery between the rigid graphite layers. The melting transition in this system is very interesting in the context of the 2D continuous melting, and in fact the melting in high-stage alkali-metal GIC's shows remarkable natures of the continuous transition,[6,12,13] such as the 2D orientational ordering above the 3D ordering temperature, the 2D to 3D crossover of ordering, and dynamical properties.[14,15] In those high-stage compounds the interlayer interaction of individual intercalant atoms is much smaller than the intralayer and substrate interactions because of the large interlayer distance between intercalant atoms, which favors the 2D character in phase transition.[16] Thus the situation is quite similar to the absorbed monolayer on graphite[17,18] although the substrate interaction in GIC's is somewhat larger.

On the other hand, stage-1 alkali-metal compounds have some different features. Firstly, intercalant atoms in stage-1 compounds are packed much closer in the in-plane and out-of-plane directions than higher stages. The in-plane and out-of-plane interatomic distances in stage-1 Rb GIC (C_8Rb), for instance, are 4.94 and 5.70 Å, respectively, which are almost equal to the interatomic distance and lattice constant of rubidium metal itself, 4.94 and 5.70 Å, respectively.[19] Such a compact packing may lead to a stronger interlayer interaction than those in high-stage compounds, which yields the stacking ordering of intercalant layers. Another feature is the simple ground-state structure; stage-1 alkali-metal (K, Rb, and Cs) GIC's have a simple in-plane (2×2) superlattice commensurate with graphite, whereas high-stage compounds generally have more complicated incommensurate domain structures.[20-26,16] The complexity of the ground state in the latter case brings some difficulty in the comphrehensive understanding of melting, although the melting itself is very typical. The in-plane superlattice in stage-1 compounds leads to definite stacking sequence due to the elastic interaction with neighboring intercalation layers, namely, the two-layer-period $\alpha\beta$ stacking in high temperatures and the four-layer-period $\alpha\beta\gamma\delta$ or three-layer-period of $\alpha\beta\gamma$ stackings at low temperatures. (Actual stacking sequences are $A\alpha A\beta A\ldots$, etc. when including the graphite layer stacking A.) The order-order phase transitions between these different stacking phases are first order. From these 3D natures of interactions it is likely to presume that stage-1 compounds do not favor the continuous melting. However, very surprisingly, in stage-1 K and Rb GIC's have been observed

some remarkable evidence of the continuous melting transition.

The first evidence of the continuous melting was reported by Nishitani *et al.*[27] for the $\alpha\beta$ solid-liquid transition in stage-1 K GIC in x-ray diffraction experiments. In a vapor pressure P_K-scan (which corresponds to the chemical potential μ scan) experiment with T_G held constant, they observed the continuous changes in potassium composition and the order parameter at the melting point pressure $P_K = P_m$, and a remarkable increase of the in-plane and out-of-plane correlation lengths ξ in the liquid as approaching P_m. These correlation lengths do not increase up to the instrumental resolution limit, but remain finite. Thus they concluded that the melting in stage-1 K GIC is weakly first order. In an alternative experiment, Minemoto and Suematsu[28,29] studied the T dependence of critical behaviors at some constant P_K's, and revealed that the melting becomes closer to second order as P_K (sequentially T_m) increases, whereas it is first order for a low P_K and T_m. Their results suggest that the gap in the first-order transition decreases with increasing P_m (and T_m). However in stage-1 K GIC, the continuous growth of ξ from the liquid to the solid phase has not been observed even for the highest P_K (and T_m) attainable in the usual control of vapor pressure.

Among alkali-metal stage-1 GIC's, rubidium compound is considered to be more favorable for the continuous melting than stage-1 K GIC because of its higher P_m, if the results of Minemoto and Suematsu can be extended to Rb GIC's. The phase transitions in stage-1 Rb GIC were first investigated by Ellenson *et al.*[30] and three phases have been reported, the $\alpha\beta\gamma\delta$ stacking solid at a low temperature, the $\alpha\beta$ stacking solid at $T \geq 721$ K and the liquid above $T_m = 747$ K, which is the same sequence of phases as stage-1 K GIC. In fact in specific-heat measurements, Robinson *et al.*[31] observed two λ-type peaks at $T = 771.5$ and 774.0 K which are strongly suggestive of the second-order transition, although the structural origin of two separated anomalies has not been understood yet.

In stage-1 Cs compound, which has a different low temperature structure, $\alpha\beta\gamma$ stacking,[32,33] the melting from the $\alpha\beta$ solid to the liquid was reported to be first order[33] without any precursive phenomenon around T_m unlike K and Rb compounds. However this experiment corresponds to a low-P_{Cs} case, and it is suggested that in a high-P_{Cs} experiment it may show a critical behavior around T_m.

In contrast, stage-1 Li GIC has a different ground state of the in-plane $(\sqrt{3}\times\sqrt{3})$ and $\alpha\alpha$ stacking structure, and recently collects peculiar interests because the compound belongs to the universality class of the 3D three-state Potts model[34,35] for which there are some theoretical controversies on the order of transition. Experimental results in neutron diffraction and calorimetry have revealed a discontinuous change in the order parameter at T_m and a strong precursive effect below T_m, indicating that the transition is weakly first order.[36,37]

The theoretical aspect of the melting transition in these stage-1 alkali-metal GIC's has been given by Bak and Domany[38] with use of the Landau-Ginzburg theory. From the symmetry of the ordered state they derived that all the transitions from the liquid to the $(2\times2)\alpha\beta$, $(2\times2)\alpha\beta\gamma$, and $(\sqrt{3}\times\sqrt{3})\alpha\alpha$ stacking solids are first order. Lee, Aoki, and Kamimura[39] extended the Landau-Lifshitz theory to a variety of C_8M structures with use of a lattice gas model, and presented the possible configurations satisfying the Landau criteria for the second-order transition, that is, $(2\times1)\alpha\beta$, $(2\times2)\alpha\bar{\alpha}$, and $(\sqrt{3}\times\sqrt{3})\alpha\bar{\alpha}$ solids, where $\bar{\alpha}$ stands for the structure in which the mass density is deficient on the α site and its minority distributes on β, γ, and δ sites. They calculated the phase diagrams of these structures by taking account of intralayer and interlayer repulsive interactions, and showed the continuous transition from the $(2\times1)\alpha\beta$ solid to the disorder phase for a small second-neighbor interlayer interaction J_2. Moreover they indicated that a much smaller J_2 results in the first-order transition from the $(2\times2)\alpha\beta$ solid to the disordered state. In a similar calculation for the in-plane (2×2) solids Miyazaki *et al.*[40] took account of the third-neighbor repulsive and attractive interactions, and obtained three types of solids with two-, three-, and four-layer-period stackings, all of which show the first-order transition to the disordered state. Thus, these calculations based on the Landau-Ginzburg theory predict the presence of a finite first-order gap at the critical point.

By contrast, the critical behavior of melting have been studied in many simplified models, among which the order-disorder transition of the 3D four-state Potts (FSP) model is particularly interesting for melting of the Rb compound, because the four configurations α, β, γ, and δ on the in-plane (2×2) superlattice correspond to four equivalent states in the FSP model. Hermmann[41] studied the 3D FSP model with use of a Monte Carlo calculation and predicted that the total energy E changes smoothly at T_m in such a way that the derivation of E diverges, so that specific heat c_v shows a very sharp peak; but they also pointed out the presence of a small first-order gap at T_m.

In this paper we have investigated in detail the crystal structures, the phase diagrams, and the critical behavior of melting ($\alpha\beta$ solid-liquid) in stage-1 Rb GIC with use of highly oriented pyrolytic graphite (HOPG) and single crystals. The present paper is organized as follows. In Sec. II we will describe the sample preparation, the *in situ* x-ray diffraction technique, and the line-shape analysis. We will present in Sec. III the complete phase diagram of Rb GIC's as a function of P_{Rb} and T_G, and the details of the crystal structures of the $\alpha\beta$ and the $\alpha\beta\gamma\delta$ solids and the liquid at high temperatures. Also, large thermal in-plane vibrations of Rb atoms at high temperatures and their anisotropic Debye-Waller factors in the plane will be discussed. In Sec. IV we will present critical behaviors of the $\alpha\beta$ solid-liquid melting in T scans at some constant P_{Rb}, the critical parameters including the interatomic distance, the order parameter, the in-plane and out-of-plane correlation lengths, etc. Two typical cases of the melting depending on P_{Rb} will be shown, i.e., the nearly continuous melting for a high P_{Rb} and the first-order

melting for a low P_{Rb}. In Sec. V we will discuss the observed behaviors of melting in connection with the 3D FSP model and the 2D-to-3D crossover effect, and also discuss the deviation of the peak temperature of the in-plane correlation length from T_m, which was observed in the off-Bragg scans. A summary and conclusions will be presented in Sec. VI.

II. EXPERIMENTAL PROCEDURE

A. Sample preparation

Samples were made by use of the usual two-zone furnace, in which the sample temperature T_G and the chemical potential μ_i can be independently controlled. μ_i is given by the vapor pressure of intercalant P_i and T_G,

$$\mu_i = k_B T_G \ln(P_i) + f(T_G) , \quad (1)$$

$$\ln(P_i) = a/T_i + b , \quad (2)$$

where $f(T_G)$ is a function of T_G, k_B is the Boltzmann constant, and the constants a and b are, respectively, -4008 K and 9.17 for rubidium metal.[42] P_i is practically controlled by the temperature of intercalant T_i.

Single-crystal (Kish) graphite and highly oriented pyrolytic graphite (HOPG) were used as host materials. HOPG is composed of microcrystals with the c axis aligned in a mosaic spread (0.5°), and the a and b axes are randomly oriented. HOPG samples in dimensions of 4×4 mm^2 were baked at 1000 °C in a vacuum of about 10^{-4} Pa for a week. A graphite sample was cleaved to a thickness of 0.2 mm which swelled up to ~0.34 mm after intercalation. This sample thickness resulted in the maximum diffraction intensity in the transmission geometry, although it corresponds to nearly twice the calculated optimum thickness $1/\mu$, where μ is the absorption coefficient[43] of the intercalated sample. Rubidium metal (purity higher than 99.99%) was handled in a glove box filled with high-purity helium gas.

Two types of sample tubes were used according to the experimental pressure of rubidium, P_{Rb}. For a low-P_{Rb} measurement was used a Pyrex ampoule, whose setup is similar to that in Fig. 1 except for the ampoule material. The ampoule wall around a graphite sample was etched to a thickness of 0.2 mm using hydrofluoric acid (HF) to minimize the background x-ray scattering from the glass. The sample was fixed at the center of the ampoule with a tantalum sample holder. Rb metal was soaked in a stainless-steel mesh placed at the upper end of the ampoule to avoid a drip of the melt.

At a high P_{Rb} (>300 Pa) experiment, an aluminum ampoule (Fig. 1) was used since Pyrex reacts severely with Rb vapor. Aluminum is the most suitable material since it possesses high resistivity against alkali metal and small absorption coefficient for x rays. The wall of the ampoule was machined to a thickness of 0.3 mm around the sample position to reduce the background scattering of x rays, and to a thickness of 0.5 mm at the midway point to obtain a thermal insulation between the upper and lower ends. A vacuum seal of the aluminum ampoule was made by electron-beam welding.

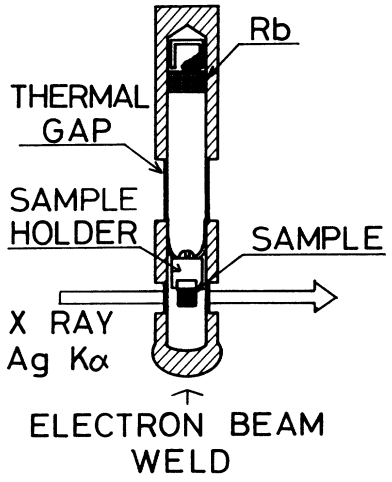

FIG. 1. A sketch of an aluminum sample tube. A graphite sample is mounted at the center of the ampoule. Rb metal is soaked in stainless-steel mesh placed at the upper end. The ampoule wall around the sample is machined to a thickness of 0.3 mm in order to reduce the x-ray absorption, and the bottom end is welded in vacuum by an electron beam.

In the present experiments a vertical, rather long two-zone furnace was used in order to ensure a wide scattering angle and to control T_G and T_{Rb} independently. For the purpose of a good spatial homogeneity of the temperatures two pieces of aluminum tubes (~3 mm thick) were placed separately at the upper (T_{Rb}) and lower (T_G) parts in the furnace. The spatial variation of temperature was ±0.5 °C/cm at the sample position so that the temperature inhomogeneity in a sample is estimated to be less than ±0.2 °C. A window for x rays was covered with thin aluminum foils to stabilize T_G. The stability of T_G and T_{Rb} was ±0.1 °C. The reaction furnace was mounted on the center of the goniometer.

B. X-ray diffraction

For x-ray diffraction experiments we used Ag $K\alpha$ radiation monochromated with a graphite crystal, which was generated from Rigaku 12-kW rotating-anode x-ray generator. Ag $K\alpha$ radiation was chosen because of its small absorption coefficient for rubidium. Dimensions of an incident collimator and slits were chosen so as to minimize the background x rays from the ampoule wall and to obtain a proper resolution. The instrumental resolution was less than 0.03 Å^{-1}.

Stage-1 Rb GIC has two solid phases with different stacking sequences, $\alpha\beta$ and $\alpha\beta\gamma\delta$. In both phases, the rubidium sublattices have the same in-plane (2×2) superlattice. In the present paper we will refer the reciprocal-lattice indices on the basis of the unit cell of the $\alpha\beta\gamma\delta$ solid hereafter. Thus the reciprocal-lattice vectors are

$$\mathbf{a}^* = \tfrac{1}{2}\mathbf{a}_0^*, \quad \mathbf{b}^* = \tfrac{1}{2}\mathbf{b}_0^*, \quad \mathbf{c}^* = \tfrac{1}{2}\mathbf{c}_0^* , \quad (3)$$

where $\mathbf{a}_0^*$ and $\mathbf{b}_0^*$ are the in-plane reciprocal-lattice vectors of graphite, and $|\mathbf{c}_0^*| = 2\pi/c_0$ ($c_0 = 5.70$ Å). The

Bragg points studied in the present work are shown in Fig. 2(a) for $\alpha\beta$ and in Fig. 2(b) for $\alpha\beta\gamma\delta$ solids. The (hkl) reflection with odd h or k comes from only the Rb sublattice. For the $\alpha\beta$ solid, the reflection with odd l disappears due to the extinction rule.

X-ray diffraction experiments were performed along some scans indicated in Fig. 3. The $(00l)$ scan was taken for monitoring the stage structure and the in-plane density of intercalants as discussed in Sec. III. In-plane structures in liquid and solids were studied by the (hkl_0) scans, l_0 being fixed at an appropriate index, while out-of-plane structures, i.e., stacking ordering, were done by the (h_0k_0l) scans. Around T_m was observed in-plane sixfold diffuse spots rather than a diffuse ring, indicating the growth of a bond-orientational correlation. The orientational correlation was observed by a rotational ϕ scan (Fig. 3) with use of a single-crystal sample.

The line-shape analysis was carried out as follows. In the liquid phase, Rb atoms have a short-range ordering with different in-plane and out-of-plane correlation lengths, ξ_a and ξ_c, respectively. The structure factor is expressed by the anisotropic Lorentzian,

$$S(\mathbf{q})=\frac{1}{1+\xi_a^2(q_a-Q_a)^2+\xi_c^2(q_c-Q_c)^2}\ , \tag{4}$$

where $S(\mathbf{q})$ is the structure factor, and $\mathbf{q}$ and $\mathbf{Q}$ are, respectively, the scattering and reciprocal-lattice point vectors. Here the suffixes a and c stand for the $\mathbf{a}^*$ and $\mathbf{c}^*$ components of a vector, respectively. The line-shape analysis for diffuse scatterings in the liquid were made by best fits to a Lorentzian after subtracting the background. In addition to the axial anisotropy, our system shows an in-plane anisotropic correlation which is characterized by the in-plane radial (ξ_a) and orientational (ξ_ϕ) correlation lengths. They were calculated from the full width at half maximum (FWHM) of radial and rotational peak profiles, respectively, after corrections of the experimental resolution and the sample mosaic spread.

In solid phases two kinds of ordering coexist; one is the quasi-2D short-range ordering due to thermal fluctuations, which gives diffuse scatterings of a Lorentzian, and

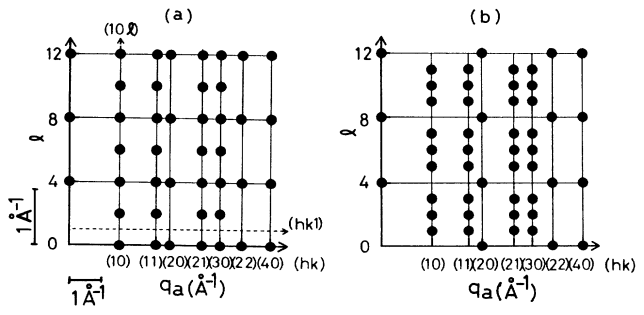

FIG. 2. Reciprocal-lattice diagram of stage-1 C_8Rb: (a) for the $\alpha\beta$ solid and (b) for the $\alpha\beta\gamma\delta$ solid. The Bragg points on diffraction planes including the $\mathbf{c}_*$ axis are plotted on the same plane.

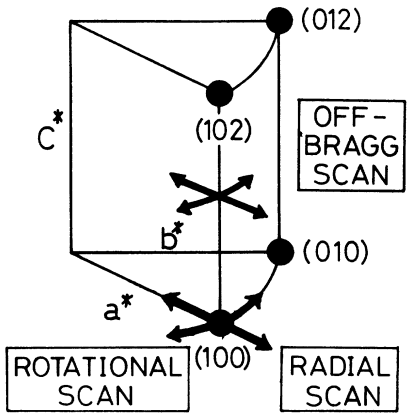

FIG. 3. Some diffraction scans for observation of diffuse scatterings. The radial and rotational scans across the Bragg point (100) and off-Bragg point (101) are shown.

the other is the long-range ordering of the $\alpha\beta$ solid, which gives Gaussian Bragg peaks. An experimental line shape was assumed to be a superposition of these two contributions. However the diffuse scattering in the on-Bragg scan, which is too weak to extract its contribution in the presence of a strong Bragg peak, is replaced by the diffuse scattering observed in the off-Bragg scan: This scan does not include the Bragg reflection of the $\alpha\beta$ solid, but gives only the sectional profile in the 2D ridge from the in-plane short-range ordering.

The structure factors at high temperatures were calculated by taking account of the anisotropic Debye-Waller (DW) factor,[44] $\exp(-2W)$,

$$\exp(-2W)=\prod_i (1-|\mathbf{q}\cdot\mathbf{U}_i|^2)\ , \tag{5}$$

and

$$W=\tfrac{1}{2}\sum_i |\mathbf{q}\cdot\mathbf{U}_i|^2\ , \tag{6}$$

where $|\mathbf{U}_i|$ is the amplitude of the vibration mode i. In the present work, we consider different DW factors in the directions of $\langle 100\rangle$ and $\langle \bar{1}20\rangle$ in order to obtain a satisfactory fit of structure factors to observed intensities.

III. PHASE DIAGRAM AND CRYSTAL STRUCTURE OF STAGE-1 Rb GIC's

A. Phase diagram of Rb GIC's

The phase diagram of Rb GIC's was obtained by means of x-ray diffraction measurements at high temperatures, which are summarized in Fig. 4. The stage structure was determined by the $(00l)$ diffraction spectra as a function of P_{Rb} with T_G fixed, while the in-plane structure, liquid or solid, was done by the (hkl_0) diffraction. In stage 1, we observe one liquid and two solid phases. The liquid phase, which is characteristic of diffuse scattering in the $(hk0)$ diffraction spectrum, exists at a high-temperature and low-pressure region. Two solid

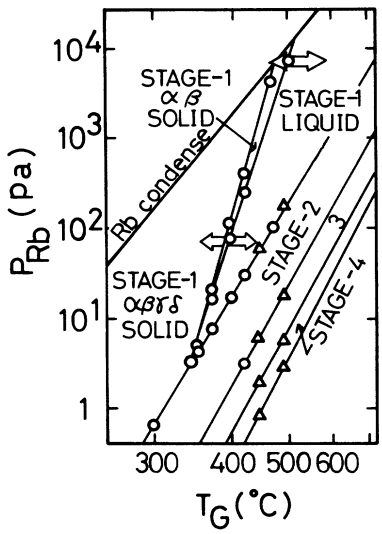

FIG. 4. The (P_{Rb},T) phase diagram of Rb GIC's. In stage-1 there are one liquid and two solid phases of different stacking sequences, $\alpha\beta$ and $\alpha\beta\gamma\delta$. Open circles stand for the phase boundary determined from the $(hk0)$ and $(10l)$ scan. Open triangles are stage transition points observed in the $(00l)$ scan. Arrows indicate two experimental T_G scans, that is, the upper corresponds to the high-P_{Rb} case ($P_{Rb}=7.7\times10^3$ Pa) and the lower to the low-P_{Rb} case ($P_{Rb}=6.1\times10$ Pa).

phases have the same in-plane unit cell with a (2×2) triangular lattice, but different stacking sequences; the low-temperature solid phase has the four-layer-period stacking $(\alpha\beta\gamma\delta)$ while the high-temperature solid phase has the two-layer-period stacking $(\alpha\beta)$. The existing region of the $\alpha\beta$ solid is restricted in a very narrow area between the liquid and the $\alpha\beta\gamma\delta$ solid. The qualitative features of this phase diagram are quite similar to those of K GIC's.[29] A quantitative difference is the intercalant pressure stabilizing the $\alpha\beta$ solid; the stabilizing pressure is $5.0\le P_{Rb}\le1.3\times10^4$ Pa for C_8Rb while it is $1.0\times10\le P_K\le8.0\times10^2$ Pa for C_8K. According to the previous results in K GIC's,[29] it is suggested that melting at a high P_i may be favorable to a smaller gap of the first-order transition, from which we may anticipate the second-order transition in C_8Rb.

From the obtained phase diagram, we deduce the enthalpy ΔH and ΔS of an intercalation reaction using the relation for a two-phase coexistence line,

$$\ln(P_{Rb}/P_0)=\frac{\Delta H}{RT}-\frac{\Delta S}{R}\ , \tag{7}$$

where P_0 is the pressure in the standard state. Experimental values of ΔH and ΔS are given in Table I. They are in good agreement with the earlier results of Salzano and Aronson[45] except for those of melting transition. In our phase diagram, the crossing point of the melting and Rb condensation lines is extrapolated at $T_m=517$ °C ($P_{Rb}=1.4\times10^4$ Pa), which corresponds to its maximum value in the ordinary condition. In fact some earlier experiments give a lower T_m than this maximum temperature; $T_m=498.3-500.8$ °C in the c_p measurement,[37] and $T_m=472$ °C in the neutron diffraction measurement.[30] However the data of Salzano *et al.* give a quite higher value ($T_m\sim730$ °C). In the experiments of Salzano *et al.* P_{Rb} was measured in a nonequilibrium condition and this experimental difficulty may bring some erroneous results, especially at higher pressures.

B. Structure of the stage-1 $\alpha\beta$ solid

Figure 5(a) shows the $(hk0)$ diffraction spectrum of the high-temperature $\alpha\beta$ solid observed at $T_G=486.0$ °C and $P_{Rb}=7.7\times10^3$ Pa. All the $(hk0)$ Bragg reflections (100), (110), (210), etc., appear in the spectrum. This fact indicates that the in-plane lattice constant of the Rb sublattice is twice that of graphite, which indicates two possibilities for the in-plane structure; the (2×2) and (2×1) in-plane superlattices. However, the possibility of the (2×1) superlattice can be excluded because the $(hk0)$ reflection of odd h or odd k should be extinct for this structure as far as $\alpha\beta$ stacking is concerned. The stacking sequence of Rb layers was determined to be of two-layer period, $\alpha\beta$, by the following facts: The Bragg peaks appear at even l in the $(10l)$ scan [Fig. 5(b)], and all the observed Bragg peaks in the (h_0k_0l) scans ($h_0,k_0=1$ or 2) reproduce the complete set of the Bragg reflections in Fig. 2(a). We concluded that this high-temperature solid phase has the (2×2) in-plane unit cell with a two-layer-stacking period; i.e., a $(2\times2)\alpha\beta$ solid.

The calculated intensities of the $(hk0)$ spectrum for a $(2\times2)\alpha\beta$ solid are in good agreement with experimental intensities as shown in Fig. 5(a). However, in this calculation we assume the Debye-Waller factor to be dependent on the crystal orientation. The calculation with no DW factor does not give a good fitting, as indicated in

TABLE I. The enthalpy ΔH and entropy ΔS of the intercalation reactions.

	Present work		Salzano *et al.* (Ref. 45)	
Reactions	ΔH (cal/mol Rb)	ΔS [cal/(mol Rb)K]	ΔH	ΔS
$\alpha\beta\gamma\delta$ solid↔$\alpha\beta$ solid	−52 236	−34.2		
$\alpha\beta$ solid↔stage-1 liquid	−45 200	−34.2	−33 900	−42.2
stage-1 liquid↔stage-2 liquid	−24 700	−23.4	−25 300	−19.2
stage-2 liquid↔stage-3 liquid	−26 600	−20.2	−27 200	−17.0
stage-3 liquid↔stage-4 liquid	−26 700	−18.2	−29 500	−17.6
stage-4 liquid↔stage-5 liquid	−29 040	−18.0	−31 100	−18.3

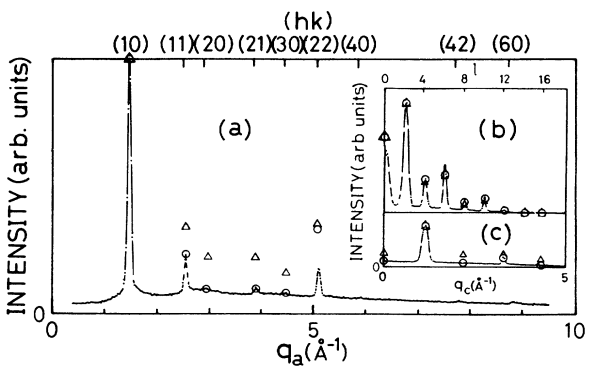

FIG. 5. (a) The ($hk0$) x-ray diffraction spectra of a stage-1 $\alpha\beta$ solid observed at $T_G=486.0$ °C and $P_{Rb}=7.7\times10^3$ Pa (HOPG-1). Open circles and triangles denote the calculated intensities with and without taking account of in-plane anisotropic DW factors, respectively. The insets show (b) the ($10l$) and (c) ($20l$) scan spectra.

Fig. 5(a). The amplitude of in-plane thermal vibrations of Rb atoms is obtained as $U((100))=0.40$ Å and $U((\bar{1}20))=0.48$ Å in the direction of $\langle 100\rangle$ and $\langle\bar{1}20\rangle$, respectively, from the best fit to the experimental intensities. Similar calculations indicate that the diffraction intensities in the out-of-plane directions [(h_0k_0l) scans] can be fitted to the calculated intensities by using the same anisotropic in-plane DW factors as those for the ($hk0$) spectrum without assuming the out-of-plane DW factor [Figs. 5(b) and 5(c)]. These results indicate that the thermal vibrations of Rb atoms are strongly restricted in the direction of graphite plane. The T_G-dependence of the amplitudes of in-plane vibrations are obtained in Fig. 6. As T_G approaches the melting temperature ($T_m=503.0$ °C for the present P_{Rb}), both $U((100))$ and $U((\bar{1}20))$ increase steeply. The fact that $U((100))>U((\bar{1}20))$ at high temperatures can be interpreted to mean that Rb atoms are more closely packed in the direction $\langle\bar{1}20\rangle$ than $\langle 100\rangle$. However, the crossover observed at a low temperature cannot be understood at present. In any case these are as large as 13% of the lattice constant ($a=4.94$ Å), and are comparable with the Lindemann formula[44] (20–25 %).

Because of the large in-plane thermal vibrations, the diffuse scatterings are observed in the ($hk0$) diffraction spectra; note a broad scattering at the foot of the (100) reflection in Fig. 5(a). They form a 2D ridge along q_c as shown in ($10l$) and ($20l$) scans [Figs. 5(b) and (c)]. These diffuse scatterings are not ascribed to liquid-phase contamination because only one phase can be allowed in our condition with constant P_{Rb} and a large enough reservoir of Rb vapor. Another possibility of sample inhomogeneity can be ruled out from the fact that the diffuse scatterings are observed from 30 °C below T_m. These diffuse scatterings can be understood in terms of a critical fluctuation associated with the melting transition, which will be discussed in Sec. IV.

C. Structure of the stage-1 $\alpha\beta\gamma\delta$ solid

The in-plane ($hk0$), and out-of-plane ($10l$) and ($20l$) diffraction spectra of the low-temperature $\alpha\beta\gamma\delta$ solid are shown in Figs. 7(a)–7(c), respectively. The data were obtained at $T_G=395.6$ °C and $P_{Rb}=6.1\times10$ Pa. In the ($10l$) scan, strong Bragg peaks are observed at $l=\pm1$, ±2, ±3, ±5, ±6, and ±7. This means that Rb layers have a four-layer stacking sequence, i.e., $\alpha\beta\gamma\delta$ stacking. The calculated intensities for the $A\alpha A\beta A\gamma A\delta$ stacking structure are in good agreement with those of experiments. However, very weak peaks (100), (110), (210), and (300), which should disappear by the extinction rule, are observed in the experiment. These peaks come from the stacking fault and/or mosaic spread effect.

Lagrange *et al.*[46] reported earlier that a C_8Rb (and also C_8K crystal is composed of three stacking-sequence domains $\alpha\beta\gamma\delta$, $\alpha\gamma\delta\beta$, and $\alpha\delta\beta\gamma$ which orient at 120° with respect to each other. In an experiment on HOPG we observe an average structure of the domains, which is represented by $\alpha\beta\gamma\delta$. In the $\alpha\beta$ solid three different

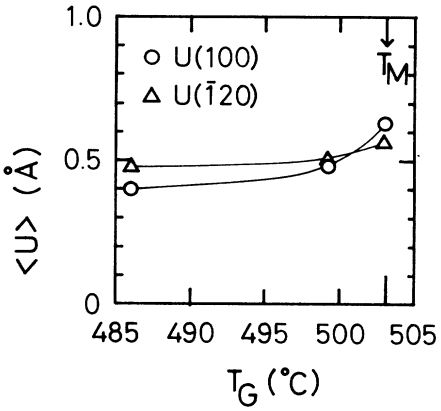

FIG. 6. The T_G-dependence of the amplitudes of in-plane thermal vibrations $U((100))$ (○) and $U((\bar{1}20))$ (△) in $\alpha\beta$ solid (HOPG-1). P_{Rb} is fixed at 7.7×10^3 Pa ($T_m=503.0$ °C).

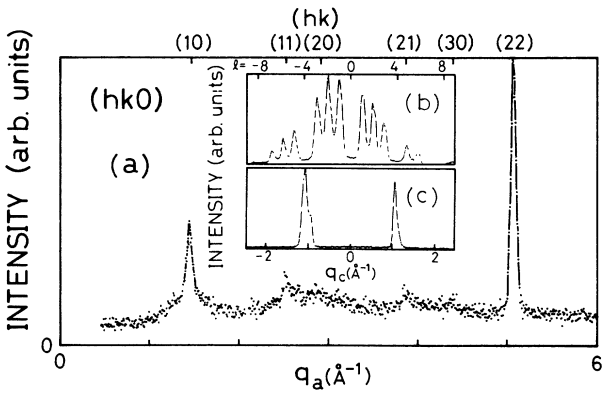

FIG. 7. (a) The ($hk0$) diffraction spectra in $\alpha\beta\gamma\delta$ solid at $T_G=395.6$ °C and $P_{Rb}=6.1\times10$ Pa (HOPG-1). The insets show (b) the ($10l$) and (c) ($20l$) scan spectra.

domains with twofold symmetry, $\alpha\beta$, $\alpha\gamma$, and $\alpha\delta$, should exist, but we observe actually the sixfold Bragg peaks as an average structure.

D. Structure of the stage-1 liquid

Figures 8(a)–8(e) show the (hkl_0) $(l_0=0,1,2,3,4)$ diffraction spectra in the liquid phase at a high temperature ($T_G=522.3\,°C$, $P_{Rb}=7.7\times10^3$ Pa) far above the critical region of melting. Three diffuse peaks observed at $q_a=1.46$, 2.83, and 4.32 Å^{-1} are, respectively, the first, second, and third diffraction halos coming from liquid Rb layers. The peak wave number of the first halo peak $q_a((100))$ $(=1.460$ Å$^{-1})$ is nearly equal to the (100) Bragg peak wave number of the $\alpha\beta$ solid, $Q_a((100))$ $(=1.467$ Å$^{-1})$. This indicates that the mean interatomic distance of rubidium in liquid is nearly equal to that of the solid, twice the in-plane lattice constant of graphite. Moreover sixfold diffuse spots are observed when a single-crystal sample is used. These spots are aligned in the directions of graphite in-plane lattice vectors. These facts indicate that a liquid Rb layer has the sixfold symmetrical correlation, i.e., the short-range ordering of the (2×2) triangular lattice.

The intensities of these halos are approximately independent of q_c, namely, each halo forms a ridge parallel to the $\mathbf{c}^*$ axis. This 2D nature of the liquid is shown more clearly in the out-of-plane diffraction spectra (Fig. 9) as a very broad peak centered at $l_0=0$. However, in addition to the broad ridge, they also show a modulated structure at $l=2n$ (n, integer) as seen in the $(10l)$ scan. The structure corresponds to a two-layer-period modulation along the $\mathbf{c}^*$ axis, and the relative intensities of the halos are quite similar to those of $\alpha\beta$ solid (see Fig. 5). Thus the short-range ordering in the liquid phase has the same symmetry as $\alpha\beta$ solid, which suggests a possibility of continuous melting in C_8Rb.

The sharp Bragg peaks in the (hkl_0) (Fig. 8), $(20l)$, and $(22l)$ scans [Fig. 9(c) and 9(d)] are the reflections from the rigid graphite lattice. The extinction rule for the observed Bragg reflections, i.e., the appearance of $l=4n$ only, indicates the $AAAA$ stacking sequence of graphite layers in stage-1 liquid;[47] the 3D rigid framework of graphite layers is conserved on the melting transition of intercalant layers.

The liquid structure mentioned above has little temperature dependence far above the critical region of melting, as shown in Fig. 8(f). By contrast, in the critical region the peak wave number of these halos shifts closer to those of the $\alpha\beta$ solid, and the peaks increase in intensity and decrease in line width as shown in Fig. 8(g).

Figure 10 shows the P_{Rb} dependence of rubidium composition m in liquid at a fixed $T_G=400.2\,°C$. The experimental data are determined from the relative intensity ratio of the $(00l)$ diffractions with use of the following relation:

$$\frac{I((001))}{I((002))}=\frac{L((001))}{L((002))}\frac{mf_C-f_{Rb}}{mf_C+f_{Rb}}\,, \tag{8}$$

where the composition m is defined as C_mRb, f_C and f_{Rb} are the atomic form factors of carbon and rubidium,[43] respectively, and $L((00l))$ is the Lorentz-polarization factor for the $(00l)$ Bragg point. The observed m decreases continuously down to the value of the solid (C_8Rb) as P_{Rb} approaches the melting point. The continuous change of m at the melting point is one of the most pronounced

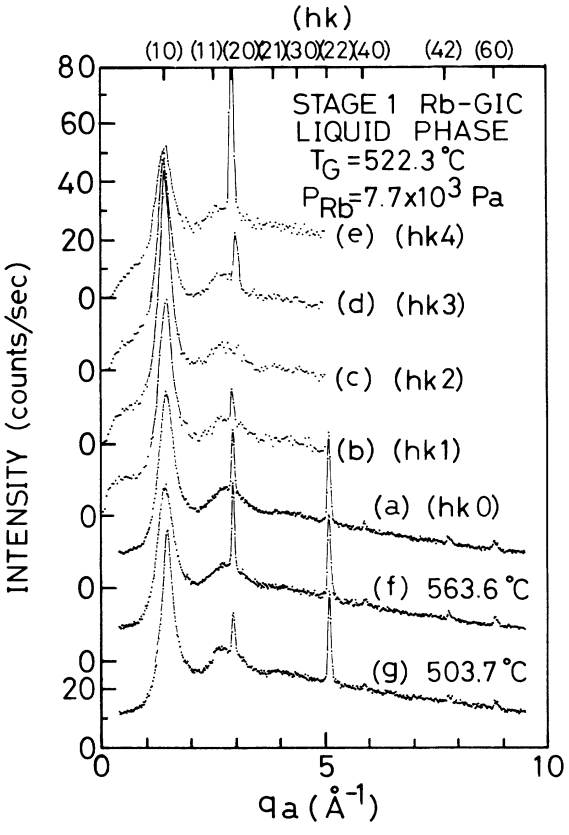

FIG. 8. The (hkl_0) x-ray diffraction spectra in liquid (HOPG-1). (a) $l_0=0$, (b) 1, (c) 2, (d) 3, and (e) 4. The spectra are obtained at $P_{Rb}=7.7\times10^3$ Pa and $T_G=522.3\,°C$, above $T_m=503.0\,°C$. The $(hk0)$ spectra at a higher temperature ($T_G=563.6\,°C$) and at the critical region ($T_G=503.7\,°C$) are also shown in (f) and (g), respectively.

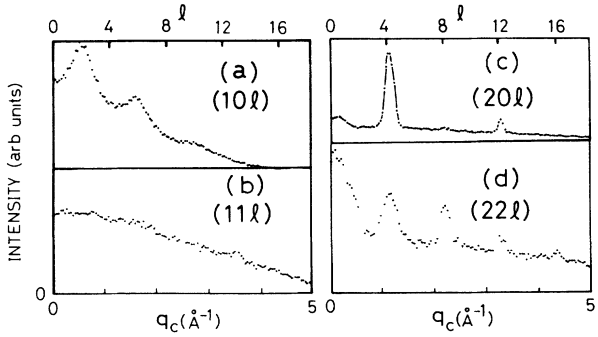

FIG. 9. The x-ray diffraction spectra in the out-of-plane directions (h_0k_0l) in liquid observed at $P_{Rb}=7.7\times10^3$ Pa and $T_G=522.3\,°C$ (HOPG-1): (a) $(10l)$, (b) $(11l)$, (c) $(20l)$, and (d) $(22l)$ scans. A two-layer-period modulation is superimposed on a broad (2D) diffuse scattering.

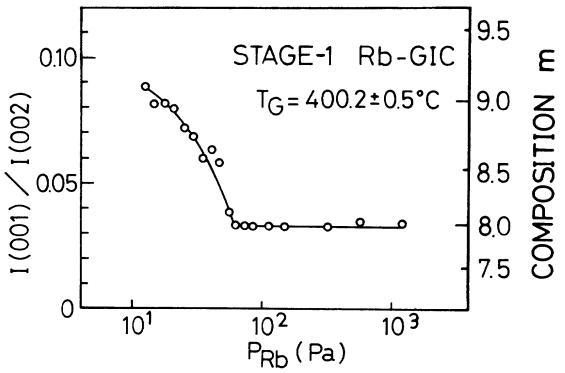

FIG. 10. The P_{Rb} dependence of Rb composition m in C_mRb at $T_G=400.2$ °C. The liquid-solid transition occurs at 63 Pa. As P_{Rb} increases m decreases smoothly from 9.2 to 8.0 while it is constant at 8.0 above 63 Pa. Note that m shows no discontinuous change at the melting point. The line is guide to the eye.

critical behaviors in C_8Rb melting, which will be discussed later.

IV. CRITICAL BEHAVIOR OF THE MELTING TRANSITION

Very recently Nishitani *et al.*[27] and Minemoto *et al.*[29] reported remarkable critical phenomena of the melting transition in C_8K. In their experiments, the nature of melting is dependent on the vapor pressure of intercalant P_K (and consequently μ_K); at a high P_K the critical behavior is characteristic of the second-order transition, while at a low P_K the transition is of first order. In the present work on C_8Rb, we have studied critical behavior of melting in a function of T_G for two typical cases of P_{Rb}, 7.7×10^3 and 6.1×10 Pa (as indicated by arrows in Fig. 4); the former is near the upper limit of P_{Rb} in the phase diagram and corresponds to the case of nearly-second-order transition, while the latter corresponds to the first-order case.

In the present experiments we have investigated critical behavior of the in-plane and out-of-plane structures, the positional and orientational correlations in the plane, the stacking correlation, and the order parameters with use of single crystal (SC-1, SC-2) and HOPG (HOPG-1) samples. Single crystals were used in order to observe the positional (radial) and bond-orientational (rotational) correlations in the plane.

A. High P_{Rb} case ($P_{Rb}=7.7\times10^3$ Pa, $T_m=503.0$ °C)

1. In-plane structure and correlations in liquid

Remarkable critical behavior of the in-plane structure is observed in the T_G dependencies of the first halo peak in the liquid ($T_G\geq T_m$) and of the (100) Bragg peak in the solid ($T_G<T_m$); Fig. 11 shows the corresponding in-plane (100)-radial and -rotational scans in SC-1 for

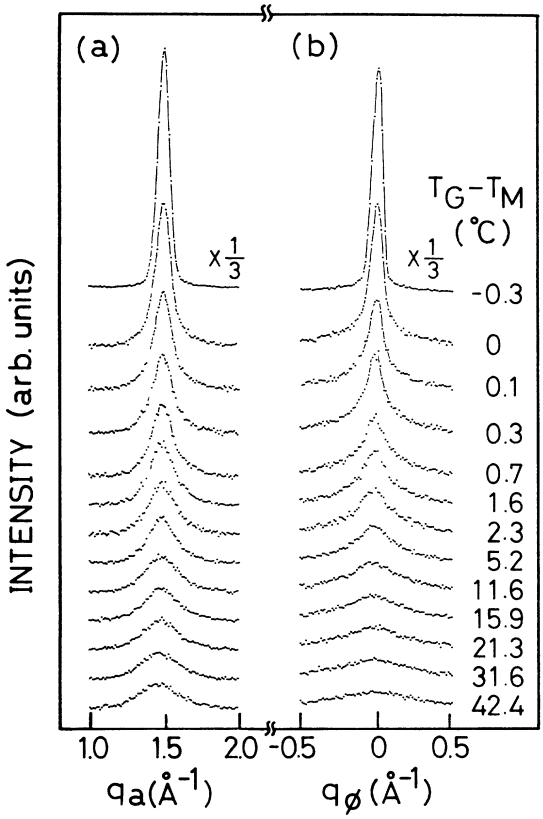

FIG. 11. The T_G dependence of (a) the (100)-radial and (b) (100)-rotational spectra in the high P_{Rb} case, $P_{Rb}=7.7\times10^3$ Pa (SC-1). The melting occurs at $T_m=503.0$ °C. The diffuse peak in liquid ($T_G>T_m$) grows continuously to the Bragg peak in the $\alpha\beta$ solid.

$P_{Rb}=7.7\times10^3$ Pa. The melting temperature T_m was determined as 503.0 °C from the onset temperature of the Bragg peak. The first halo peak of liquid appears at a wave number $q_a((100))$ nearly equal to $Q_a((100))$. This diffuse scattering has the sixfold anisotropy in intensity with the maximum aligned to the graphite lattice vector [Fig. 11(b)]. These features indicate that liquid Rb has a short-range-ordering of the in-plane (2×2) triangular lattice. As T_G comes down to T_m, the diffuse peaks of liquid increase in intensity and decrease in linewidth, and seem to continue to the Bragg peak of the $\alpha\beta$ solid. Eventually, $q_a((100))$ coincides with the value of $Q_a((100))$ $(=1.467$ Å$^{-1})$ at T_m, while $q_\phi((100))$ shows no change through the melting transition as shown in Figs. 12(a) and 12(b). Below T_m the Bragg peak grows steeply with decreasing T_G. We note here an important feature that q_a and q_ϕ change continuously at T_m within experimental error; that is, the mean atomic distance and bond-orientation of Rb atoms have no discontinuous change at T_m.

The T_G dependence of in-plane radial and rotational correlation lengths $\xi_a((100))$ and $\xi_\phi((100))$, respectively, are shown in Fig. 13. At a high temperature far above

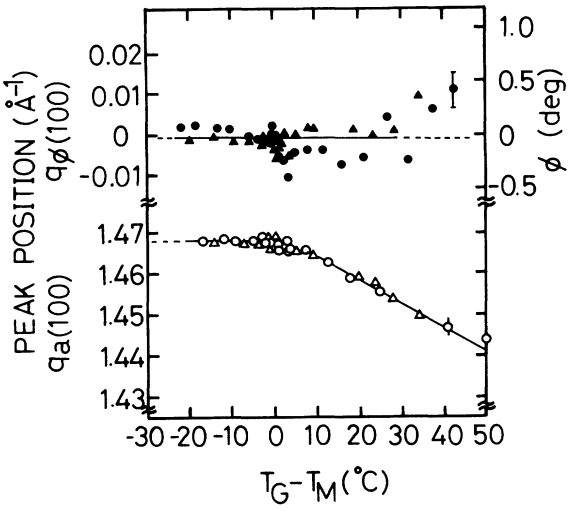

FIG. 12. The T_G dependence of the peak wave numbers (a) $q_a((100))$ and (b) $q_\phi((100))$. Circles and triangles are obtained in heating and cooling runs, respectively. $q_a((100))$ and $q_\phi((100))$ neither show a discontinuous change nor thermal hysteresis at T_m.

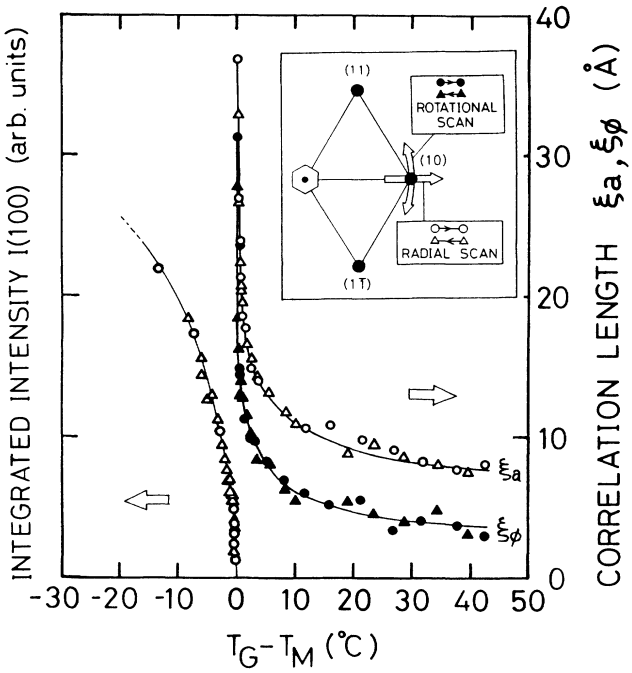

FIG. 13. The T_G dependence of in-plane correlation lengths $\xi_a((100))$ and $\xi_\phi((100))$ in liquid in the high P_{Rb} case (SC-1). The solid curves are power law fits for the critical exponents $\nu_a=0.24$ and $\nu_\phi=0.34$. The T_G dependence of the integrated intensity of the (100) Bragg peak, $I((100))$, is also shown below T_m. T_m is determined by the onset temperature of $I((100))$. The solid line is power law fit for $2\beta=0.60$. The inset shows the paths of the scattering vector in the radial and rotational scans.

T_m (e.g., $T_G-T_m=43$ °C) the liquid has only a short-range ordering with $\xi_a((100))=7$ Å and $\xi_\phi((100))=3$ Å, but as T_G approaches T_m, $\xi_a((100))$ and $\xi_\phi((100))$ grow remarkably and increase up to 40 Å. The higher-order halos of the liquid grow up to individual diffraction peaks corresponding to the Bragg peaks for the (2×2) superlattice [Fig. 8(g)], which indicates the growth of the strong correlation with the symmetry of the $\alpha\beta$ solid. This critical behavior is characteristic of the second-order transition. However $\xi_a((100))$ and $\xi_\phi((100))$ remain at a finite value at T_m, smaller than the value for long-range ordering. Similar results of correlation length are also observed in HOPG-1 although $\xi_a((100))$ ($\lesssim 12$ Å) is shorter than those of single-crystal samples; the smaller value of $\xi_a((100))$ may be ascribed to a smaller domain size of HOPG.

2. *In-plane correlations in the solid*

The diffuse scattering in a solid phase, if it is observed on the Bragg point, is merged into the strong Bragg reflection. In order to extract the in-plane diffuse scatterings in solid, we have observed the off-Bragg reflection spectra in the (103)-radial and -rotational scans (Fig. 14). The T_G dependence of the in-plane correlation lengths $\xi_a((103))$ and $\xi_\phi((103))$ are shown in Fig. 15. $\xi_a((103))$ and $\xi_\phi((103))$ increase appreciably in both sides of solid and liquid phases when T_G approaches T_m, so that the ξ's have a maximum value (30 Å) around T_m. However, the critical peak of $\xi(T)$ observed in the off-Bragg scan is small and not so sharp as the peak in the on-Bragg scans. This difference of features between the on- and off-Bragg scans is plausibly ascribed to the line-shape analysis; in the analysis of the off-Bragg scans we ignored the term $\xi^2_c(q_c-Q_c)^2$ in Eq. (4), although it becomes unnegligible for a large ξ_c near T_m.

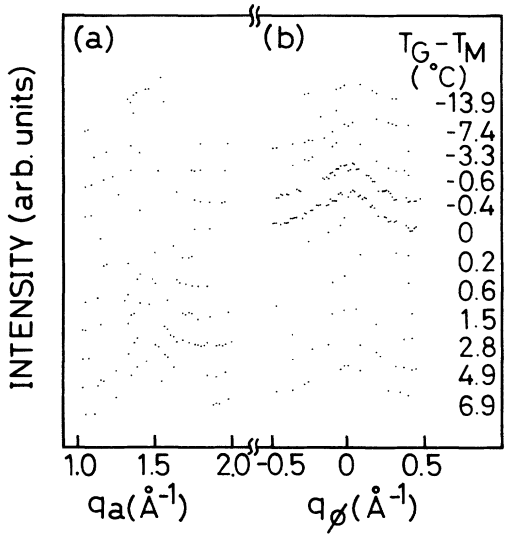

FIG. 14. The T_G dependence of the (103) off-Bragg spectra at $P_{Rb}=7.7\times10^3$ Pa (SC-1) in (a) (103) radial and (b) (103) rotational scans.

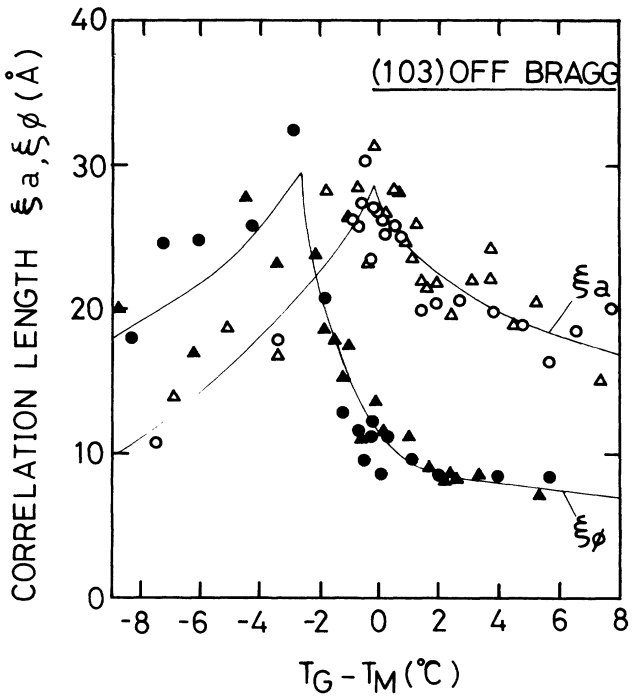

FIG. 15. The T_G dependence of in-plane correlation lengths $\xi_a((103))$ and $\xi_\phi((103))$ at $P_{Rb}=7.7\times10^3$ Pa (SC-1). The curves are guide to the eye. T_m is determined from the onset temperature of the Bragg peak of $\alpha\beta$ solid. The data on cooling (triangle) and heating (circle) runs are plotted.

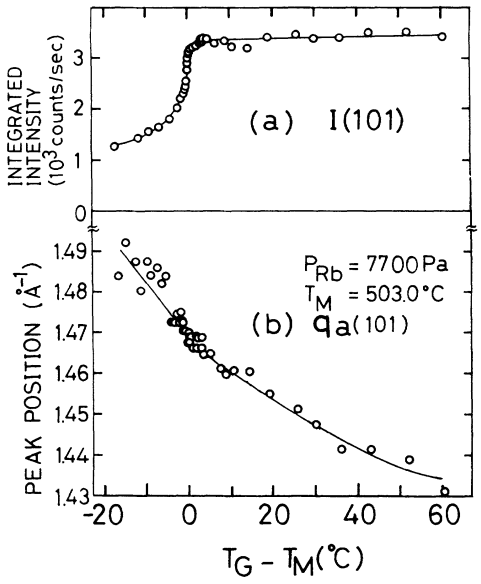

FIG. 16. The T_G dependence of the integrated intensity of (a) the (101) diffuse peak, $I((101))$, and of (b) the in-plane peak wave number $q_a((101))$ at $P_{Rb}=7.7\times10^3$ Pa (HOPG-1).

In SC-1 the peak temperature T_p of $\xi_\phi((103))$ is found to be 2.7 °C lower than T_m whereas the peak of $\xi_a((103))$ is observed at T_m. This discrepancy is not ascribed to the experimental error of the T_G-measurement, since we alternated two measurements of the on-Bragg and off-Bragg scans for each T_G point, and from the former T_m is determined. In SC-2, T_p in $\xi_a((101))$ falls at T_m within ±0.1 °C, the experimental accuracy. In HOPG-1 (in which ξ_ϕ cannot be observed due to its in-plane powder structure) $\xi_a((101))$ shows a similar shift of $T_p=T_m-1.5$ °C.[48] The phenomenon seems to be dependent on a sample, and will be discussed in Sec. V.

In Fig. 16(a) is shown the T_G dependence of the integral intensity of the (101) diffuse scattering $I((101))$ obtained in the $(hk1)$ scan for HOPG-1. The $I((101))$ increases divergently immediately below T_m: This means that the in-plane thermal vibrations of Rb atoms increase steeply, and the 3D ordering of solid is being destroyed. At a temperature above T_m ($T_G \geq T_m+5$ °C), $I((101))$ is nearly constant, which indicates that the 2D correlation of liquid is predominant at these temperatures. A similar divergent increase of $I((101))$ is observed in SC-2.

The in-plane wave number $q_a((101))$ of the 2D ridge peak [Fig. 16(b)] shows a remarkable increase in the liquid phase as T_G approaches T_m, and coincides with the Bragg peak of the $\alpha\beta$ solid $Q_a((100))$ ($=1.467$ Å^{-1}) at T_m, the feature being quite similar to the case of $q_a((100))$ for $T_G \geq T_m$. However, the $q_a((101))$ increase is still larger below T_m; namely, the peak wave number of the diffuse scattering becomes larger than $Q_a((100))$. A similar feature is implicitly observed in the $(hk0)$ diffraction spectrum, in which the line shape of the diffuse scattering shifts appreciably to a larger wave number relative to the superimposed Bragg peak.

3. *Out-of-plane correlations in liquid*

The critical phenomena are also observed in the T_G dependence of the out-of-plane diffraction spectra. Figure 17 shows the $(10l)$ diffraction spectra above and below T_m in HOPG-1, which shows a remarkable increase of stacking correlations ($l=2n$) with a two-layer period near T_m. The T_G dependence of the stacking correlation length $\xi_c((102))$ is shown in Fig. 18. In the liquid phase $\xi_c(102)$ which is 3 Å at a high temperature, increase continuously up to 11 Å at T_m. In SC-2, $\xi_c((102))$ grows up to 16 Å. Thus, the stacking correlation also grows as T_G approaches T_m. This means that the 3D correlation grows simultaneously to the growth of the in-plane correlations. However, the line width does not reach the width of a Bragg peak at T_m, indicating the presence of a small first-order gap.

4. *Order parameter*

Finally, we present the behavior of the order parameter below T_m. Figure 19 shows the T_G dependence of the intensity of the (100) Bragg peak $I((100))$, which is integrated in three principal directions in the reciprocal-lattice space: $I((100))$ is proportional to the square of the order parameter of the $\alpha\beta$ solid. The intensity $I((100))$ begins to increase continuously at T_m and shows

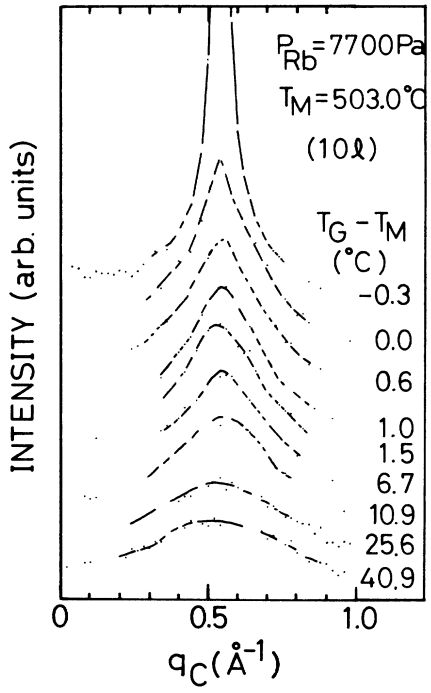

FIG. 17. The out-of-plane (10l) diffraction spectra observed at $P_{Rb}=7.7\times10^3$ Pa (HOPG-1) as a function of T_G. The stacking correlation of $\alpha\beta$ solid grows continuously across T_m.

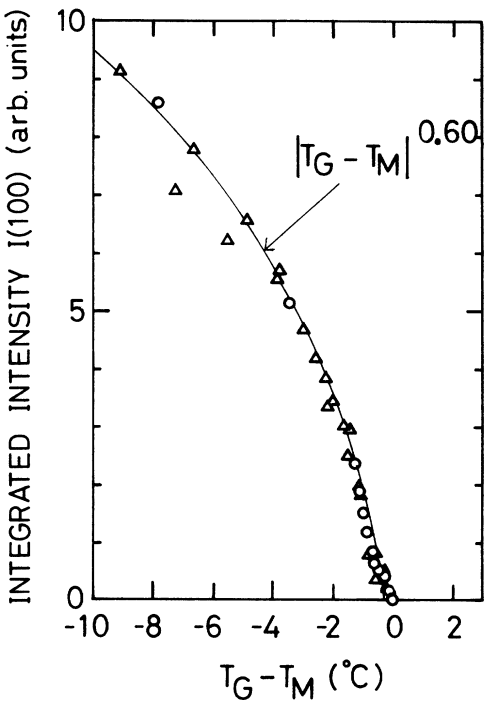

FIG. 19. The T_G dependence of the integrated intensity of the (100) Bragg peak of $\alpha\beta$ solid $I((100))$ at $P_{Rb}=7.7\times10^3$ Pa (SC-1). The solid line is a power-law fit with a critical exponent $2\beta=0.60$.

neither appreciable discontinuous change nor thermal hysteresis within our experimental accuracy. The increase of $I((100))$ below T_m can be fitted to a power law, $I((100))\sim t^{2\beta}$ in a satisfactory accuracy, where the critical exponent β is obtained as 0.30 ± 0.06, and $t=(T_m-T_G)/T_m$, T_m being the onset temperature of the Bragg peak.

The critical phenomena mentioned above are obtained for $P_{Rb}=7.7\times10^3$ Pa which is a little lower than the condensation pressure of Rb; $T_{Rb}=T_m$. However, essentially the same features are observed for nearly limiting pressures, $P_{Rb}=9.6\times10^3$ Pa ($T_m=510$ °C) and 1.2×10^4 Pa ($T_m=515$ °C): The critical parameters $q_a((100))$, $\xi_a((100))$, and $I((100))$ show a continuous change at T_m, and the correlations growing in liquid have the same symmetry as that of the $\alpha\beta$ solid, but ξ_a and ξ_c remain finite at T_m. These features are essential and quite reproducible for melting for $P_{Rb}\geq6.6\times10^3$ Pa.

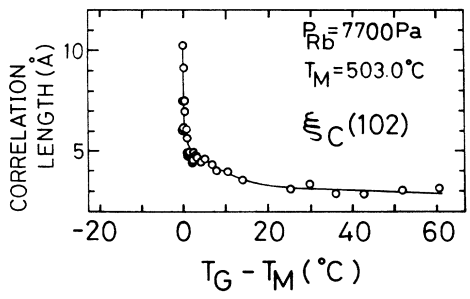

FIG. 18. The T_G dependence of stacking correlation length $\xi_c((102))$. The data are obtained from Fig. 17. The line is guide to the eye.

B. Low-P_{Rb} case ($P_{Rb}=6.1\times10$ Pa)

In contrast to the high-P_{Rb} case discussed above, the melting transition at a low P_{Rb} is found to be of first order. We show a typical result obtained at $P_{Rb}=6.1\times10$ Pa, the pressure corresponding to the midpoint between the upper and lower limits of T_{Rb} for the stage-1 melting. As shown in Fig. 20(a), the T_G-dependence of $q_a((100))$ shows a large discontinuity at T_m between the liquid (1.40 Å^{-1}) and solid phases (1.46 Å^{-1}), which means that the in-plane density of Rb atoms change discontinuously at T_m. The in-plane correlation length $\xi_a((100))$ increase to 8 Å immediately below T_m from 5 Å far above T_m, which is indicative of the precursive phenomena of melting, but a critical increase is not observed around T_m [Fig. 20(c)]. A similar discontinuity is observed in the order parameter [Fig. 20(b)]. The integral intensity $I((100))$ of the $\alpha\beta$ solid shows a large discontinuity at T_m, associated with a small thermal hysteresis of about 0.2 °C. These features indicate that the melting in a low P_{Rb} case is the first-order transition. The pressure dependence of the nature of the melting in stage-1 Rb GIC is quite similar to that in the stage-1 K GIC.[28,29]

For a low P_{Rb} case, we observed a structural phase transition from an $\alpha\beta$ to an $\alpha\beta\gamma\delta$ solid at a temperature

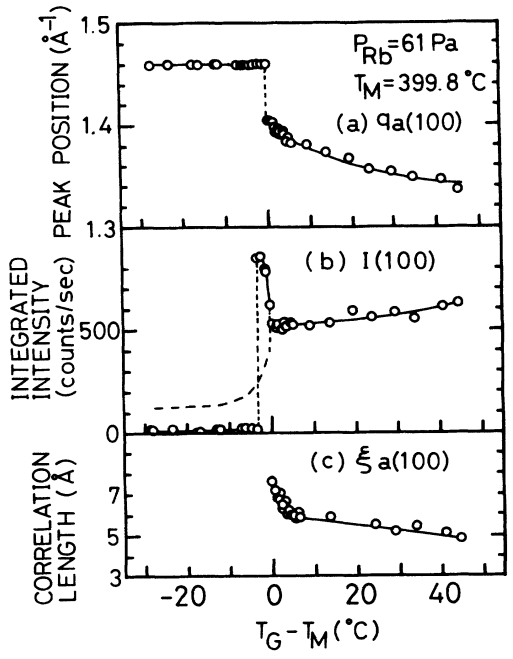

FIG. 20. The T_G dependencies of (a) $q_a((100))$, (b) $I((100))$, and (c) $\xi_a((100))$ at $P_{Rb}=6.1\times10$ Pa, the low-P_{Rb} case. The melting occurs at $T_m=399.8$ °C. A large discontinuity is observed in $q_a((100))$ and $I((100))$, while no critical behavior is observed around T_m.

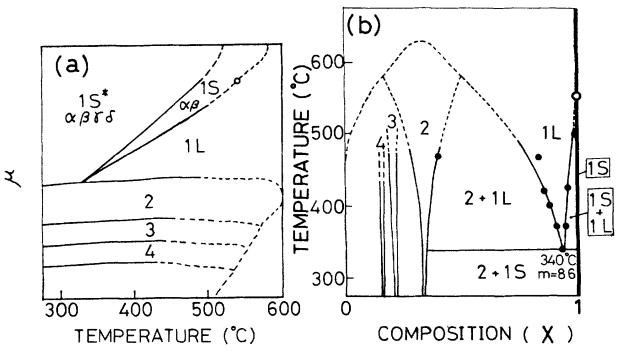

FIG. 21. The complete phase diagram of Rb GIC's, in (a) (μ,T) and (b) (x,T) sections. Experimental points determined by x-ray diffraction are plotted. (○) denotes hypothetical critical point, and dotted lines are estimated phase boundaries according to the theoretical calculation by Safran *et al.* (Ref. 8).

below T_m. This structural transition is accompanied with a large discontinuity of $I((100))$ and a thermal hysteresis of about 0.5 °C [which are seen at 397 °C in Fig. 20(b)]. We conclude that this stacking transition from $\alpha\beta$ to $\alpha\beta\gamma\delta$ is of first order.

V. DISCUSSION

A. Phase diagram and the P_{Rb} dependence of the melting nature

The phase diagram in the (P_{Rb},T) section for Rb GIC's is quite similar to that of the K GIC's. However, the liquid-solid boundary for the Rb system shifts towards the high-temperature and high-pressure side, and the existing region of the $\alpha\beta$ solid is broader compared with the K GIC's. The corresponding (x,T) section for Rb GIC's has been determined from x-ray structural studies in a crude approximation; the atomic composition x of Rb (relative to C_8Rb) was deduced from the intensity of $(00l)$ reflections according to Eq. (8) and/or the peak wave number of the first halo peak $q_a(100)$ in liquid. The (x,T) and (μ,T) sections of the phase diagram for Rb GIC's are shown in Figs. 21(a) and 21(b), respectively. The $\alpha\beta$ solid phase appears above the eutectic temperature $T_e=340$ °C, which corresponds to the coexistence point of the stage-1 liquid, stage-1 solid, and stage-2 liquid phases.

The critical nature of melting changes with P_{Rb} (consequently T_m). For a T_m near T_e, the transition is obviously first order, but with increasing T_m the first-order gap decreases and eventually appears to be zero as far as the order parameter and the rubidium density are concerned: These phenomena are the common features for both stage-1 Rb and K GIC's. The correlation lengths ξ_a, ξ_ϕ, and ξ_c at T_m are also an increasing function of P_{Rb}, but remain finite even for the highest P_{Rb} studied here. We can point out a possibility that the second-order transition may be realized for higher P_{Rb} and T_m than the condensation temperature of rubidium (above the condensation line in Fig. 4), which will be attainable in a high pressure experiment, for instance. Such a p_i (or μ_i) dependence of the critical properties should be reexamined in an extended theory taking account of the grand canonical ensemble.

Some earlier experiments reporting the first-order transition for melting of C_8Rb may be reconsidered in the light of the present phase diagram. Chabre *et al.*[49] observed a large discontinuous change and thermal hysteresis in the susceptibility χ, and ^{38}Rb NMR Knight shift at $T_m=292-312$ °C. The observed value of T_m is about 40 °C lower than our eutectic point; it is too low for the stage-1 melting transition. The observed discontinuous change in their experiments may arise from some other phase transition such as the stage transition between stage-1 and stage-2.

For the melting in stage-1 Cs GIC Caswell *et al.*[32] concluded the first-order transition from discontinuous changes observed in atomic density and in-plane wave number $q_a((100))$. However, Caswell's experiment was made at a rather low P_{Cs}, not far from the eutectic point in the phase diagram of Salzano and Aronson.[50–53] We may expect another result for stage-1 Cs GIC at a higher P_{Cs}, although the present K and Rb results cannot be directly applied to the case of stage-1 Cs-GIC since it has the different ground state ($\alpha\beta\gamma$ stacking structure) unlike that of K and Rb GIC's.

B. Critical behavior

The melting transition in stage-1 Rb GIC at a high P_{Rb} shows continuous change, at T_m, of critical behavior,

namely the in-plane interatomic distance, the bond-orientation, and the order parameter, all of which accompany no thermal hysteresis. The melting is furthermore associated with strong critical fluctuations above and below T_m. The correlation of the fluctuations in liquid has the same symmetry as the low-temperature $\alpha\beta$ solid phase and grows remarkably around T_m in the in-plane radial and in-plane angular directions, and the out-of-plane direction.

Some experimental results indicate that these correlations have noticeable 2D characters except for the narrow T_G region close to T_m; namely, the diffuse scattering, which forms a rather sharp peak in the in-plane direction, elongates like a ridge along the **c*** axis, and the integrated intensity of the ridge remains constant down to a few degrees above T_m [Fig. 16(a)]. Moreover, as is shown in Fig. 22, the ratio of out-of-plane to in-plane correlation ξ_c/ξ_a is fairly small (~ 0.5) at higher temperatures ($T_G \geq T_m + 10\,^\circ\mathrm{C}$). These facts mean that the 2D short-range order is predominant at high temperatures. However it cannot grow up to the 2D long-range order in the real system.

Around T_m, ξ_c becomes comparable with ξ_a, and the 2D-to-3D crossover is observed. The critical exponent of order parameter β is found to be 0.30 ± 0.06, which is nearly equal to the calculated values for 3D systems using the renormalization-group theory,[54] i.e., $\beta=0.31$ for 3D Ising, 0.33 for 3D XY, and 0.38 for 3D Heisenberg systems. The fact suggests that the 3D interaction is responsible for the long-range ordering of Rb sublattice in the vicinity of T_m. Thus we can obtain a simplified picture for the ordering process: The 2D short-range order grows first at high temperatures, and with decreasing temperature the 2D correlation increases sufficiently large so that the 3D correlation grows due to interlayer interaction between 2D correlated clusters, and eventually the 3D long-range order appears at T_m.

The temperature dependence of in-plane correlations can be expressed by one critical exponent in the temperature region of $10^{-4} < t < 10^{-1}$ above T_m as shown in Fig. 23,

$$\xi \sim t^{-\nu}, \quad t=(T-T_c)/T_c \ , \tag{9}$$

where the critical exponent ν_a is found to be 0.24 ± 0.04 for ξ_a and $\nu_\phi=0.34\pm0.04$ for ξ_ϕ. Here the critical temperature T_c is assumed to be $T_m-0.2\,^\circ\mathrm{C}$ for best fits.

Now we will discuss this critical behavior comparing with the existing theories. The present case of melting transition does not correspond to any case of the second-order transition proposed for stage-1 GIC's by Lee *et al.*,[39] in which only three kinds of structures, $(2\times1)\alpha\beta$, $(2\times2)\alpha\bar{\alpha}$, and $(\sqrt{3}\times\sqrt{3})\alpha\bar{\alpha}$ are allowed, so that the present transition should be first order in the symmetrical consideration. In fact the observed ξ's remain finite at T_m, shorter than the value of long-range ordering apart from the continuous nature of the other critical properties.

However in these works based on the Landau theory we cannot obtain the exact picture for critical behavior above and below T_m. These critical problems of melting have been studied so far in many statistical calculations. An interesting case is the calculation for the four-state Potts (FSP) model[34,35] since the (2×2) superlattice in C_8Rb has four equivalent configurations α, β, γ, and δ, which correspond to the 3D FSP model.[55] The critical behaviors in the 3D FSP model have been studied by Hermmann[41] with use of Monte Carlo calculation. He showed that the energy of system E changes nearly continuously close to T_c but has a small discontinuous gap at T_c, while specific heat c_v has a large and sharp peak at T_c and ξ_a has a critical exponent of $\nu=0.33\sim0.52$. The calculated ν is comparable to the present values of 0.34 ± 0.04 for ξ_ϕ and 0.24 ± 0.04 for ξ_a, and the observed specific heat shows a λ-type anomaly at T_m.[31] Further-

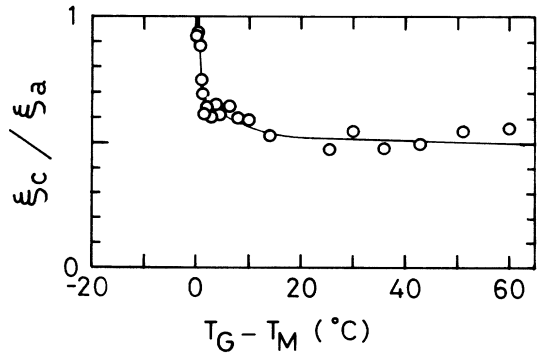

FIG. 22. The T_G dependence of the ratio of out-of-plane to in-plane correlations ξ_c/ξ_a at $P_{Rb}=7.7\times10^3$ Pa.

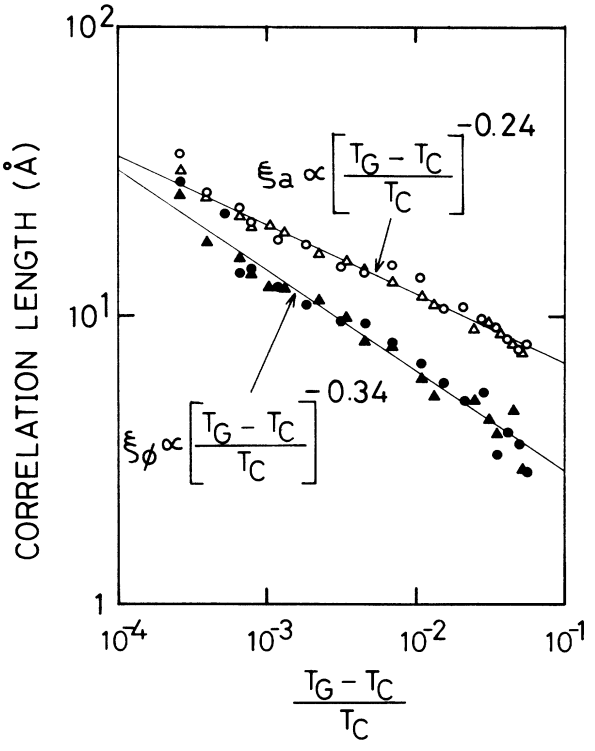

FIG. 23. The log-log plots of correlation lengths $\xi_a(100)$ and $\xi_\phi(100)$ vs reduced temperature t.

more, the system shows some strong features of the second order transition. Thus the calculated results are in good qualitative agreement with the experimental results in C_8Rb. The predicted discontinuous gap cannot be ruled out by our experimental results because it may be undetectably small.

On the other hand, Nelson *et al.*[56] and Young[57] predicted the Kosterlitz and Thouless (KT) type transition[58] for melting of the 2D system on a hexagonal potential. In this case the correlation length is represented by the formula

$$\xi_a \sim \exp(Bt^{-\mu}), \quad t=(T_G-T_{\rm KT})/T_{\rm KT}\ , \tag{10}$$

where the calculated exponent μ is dependent on the intensity of the substrate potential and ranges between 0.37 and 0.4, and B is a constant value. However the experimental data of ξ_a could not be fitted to Eq. (10).

We will discuss briefly the deviation of the peak temperature T_p of ξ from T_m, which is observed in the off-Bragg scans. The phenomenon seems quite strange since in the usual system ξ has the maximum value at T_m due to critical fluctuations. Particularly in SC-1, only ξ_ϕ shows such a deviation of T_p whereas the other critical parameters including ξ_a show anomalies at T_m. Similar anomalies have been observed in c_p measurements by Robinson *et al.*[31] who obtained two λ-type peaks at 771.5 and 774.0 K. The temperature difference between the anomalies, $\Delta T=2.5$ K, is very close to $\Delta T=2.7$ K in our case: The difference of the absolute value T_p (or T_m) between the two experiments may arise from the difference of the experimental conditions. We mentioned that the anomaly at T_p does not come from some instrumental problem but may be intrinsic to the melting in C_8Rb. However, we have not understood the experimental details such as the accurate temperature dependence of ξ in the off- and on-Bragg scans and the sample dependence, so that we can give some possible speculations at present.

(1) One possibility is related to the surface (or grain boundary) melting which may occur at a low temperature preceding the 3D melting in bulk.[59]

(2) Another possibility is that T_p corresponds to the asymptotic critical temperature T_{2D} of the 2D in-plane fluctuations discussed earlier. In this case the 2D fluctuations are the most pronounced at T_{2D}, but the 2D ordered state is energetically a little higher than the 3D ordered state so that the former state is not realized. However these possibilities (1) and (2) are difficult to explain the difference of behaviors between ξ_a and ξ_ϕ.

(3) The different temperature dependences of ξ_a and ξ_ϕ remind us a possibility of the orientational ordering ("hexatic phase") proposed for the 2D continuous melting.[56,57] In the usual theory, however, ξ_ϕ is expected to diverge at a temperature higher than the 2D translational-ordering temperature, which is contrary to the experimental results.

(4) Another structural problem is that the diffuse scattering in the off-Bragg scan is not necessarily the same as that in the on-Bragg scan, and the scattering around (101) or (103) may arise from an instability of a different structure such as a four-layer-period structure. This idea brings another unresolved problem why the new structure is unstable. Thus, we have not obtained a conclusive explanation, and the problem is still open for discussions at present.

VI. SUMMARY AND CONCLUSIONS

In this paper we have investigated the comprehensive studies of the phase diagram, the high-temperature structures of liquid and solid phases, and the critical behavior of the melting transition in stage-1 Rb GIC, with use of the x-ray diffraction.

(a) The phase diagram of Rb GIC's is determined in detail in the $(P_{\rm Rb},T)$ section, while the (x,T) section is discussed qualitatively. In stage-1 Rb GIC a liquid and two types of solid phases are observed; the solid phases are the two-layer-period stacking $\alpha\beta$ solid at a high temperature and the four-layer-period stacking $\alpha\beta\gamma\delta$ solid at a low temperature, both of which have the same in-plane (2×2) superstructure. The liquid phase exists in the high T_G and low-$P_{\rm Rb}$ region, and the $\alpha\beta$ solid exists in a very narrow region between the liquid and the $\alpha\beta\gamma\delta$ solid. The melting temperature T_m is an increasing function of $P_{\rm Rb}$. The features of the phase diagram are qualitatively the same as those of the K GIC's[27–29] although the existing region of $\alpha\beta$ solid of K GIC's is much narrower than that of Rb GIC's. From the $(P_{\rm Rb},T)$ phase diagram the enthalpy and entropy of reactions for (stage-1 liquid) $\leftrightarrow$ ($\alpha\beta$ solid), ($\alpha\beta$ solid) $\leftrightarrow$ ($\alpha\beta\gamma\delta$ solid), and stage transitions are determined.

(b) The Bragg reflection intensities in the $\alpha\beta$ solid are in good agreements with the calculated intensities assuming the in-plane anisotropic Debye-Waller factors for Rb atoms. The mean amplitude of thermal vibrations $\langle U\rangle$ at $T_G=502.7\,^\circ$C ($=T_m-0.3\,^\circ$C) is obtained as 0.63 Å in the direction $\langle 100\rangle$ and 0.56 Å in the direction $\langle \bar{1}20\rangle$. The amplitudes are dependent on T_G, particularly close to T_m, and increase by as much as 13% of the interatomic distance at 0.3 °C below T_m, which is comparable with the value of Lindemann melting formula. On the other hand the DW damping effect in the out-of-plane direction is negligibly small. These results indicate Rb atoms have large thermal vibrations strongly restricted in the direction of graphite plane.

(c) In the $\alpha\beta\gamma\delta$ solid the observed intensity of Bragg peaks agrees with the calculated intensity for the $A\alpha A\beta A\gamma A\delta$ stacking structure. No other crystal structure such as in-plane (2×1) superstructure or $\alpha\beta\gamma$ stacking structure is observed in the region studied here, i.e., $0.5\le P_{\rm Rb}\le 1.4\times10^4$ Pa and $300\le T_G\le 560\,^\circ$C.

(d) In the liquid phase a series of diffuse peaks of Rb layers are observed in the in-plane $(hk0)$ diffraction spectra. The first diffuse peak has an in-plane peak wave number $q_a((100))$ nearly equal to $Q_a((100))$, and the in-plane sixfold modulation in intensity. In the out-of-plane direction it forms a broad ridge in superposition of the two-layer-period modulation. These facts indicate that a liquid Rb layer has the short-range-ordering correlation of the in-plane (2×2) triangular lattice and also the weak two-layer-period stacking correlation, that is, the same

symmetry as the $\alpha\beta$ solid. However, a rubidium layer behaves as a quasi-2D liquid at much higher temperatures above T_m. The in-plane atomic density of Rb changes from $m=9.2$ at the phase boundary of stage-1 and -2 GIC's to $m=8.0$ near T_m.

(e) The critical nature of the melting depends on P_{Rb}, and is characteristic of the second-order transition at a high P_{Rb} while it is first order at a low P_{Rb}: The gap of the first-order transition is a decreasing function of P_{Rb}.

In the high-P_{Rb} case ($P_{\mathrm{Rb}}=7.7\times10^3$ Pa, $T_m=503.0$ °C) we have observed remarkable critical features of melting as follows: (1) $q_a((100))$ in liquid increases continuously with decreasing temperature and coincides with $Q_a((100))$ at T_m, while the peak direction remains parallel to the graphite lattice vectors through melting transition. That is, the mean atomic distance and bond-orientation of a rubidium layer have no discontinuous change at T_m. (2) The in-plane radial and bond-orientational correlation lengths in liquid, $\xi_a((100))$ and $\xi_\phi((100))$, increase steeply up to 40 Å when T_G approaches T_m from either side. The critical exponents of ξ_a and ξ_ϕ are obtained as $\nu_a=0.24\pm0.04$ and $\nu_\phi=0.34\pm0.04$, respectively. (3) The diffuse scatterings due to critical fluctuations are also observed in $\alpha\beta$ solid below T_m. ξ_a has the maximum value at T_m, but ξ_ϕ at $T_p=T_m-2.7$ °C in SC-1. HOPG-1 also shows the deviation of T_p from T_m, $T_p=T_m-1.5$ °C. The discrepancy between T_p and T_m is still open for discussions at present. (4) The out-of-plane correlation length $\xi_c((102))$ in liquid increases continuously up to 16 Å at T_m. (5) In-plane and out-of-plane correlation lengths remain at a finite value at T_m, smaller than the value for long-range ordering. (6) The integrated intensity of the Bragg peak $I((100))$, in the $\alpha\beta$ solid increases continuously below T_m. The order parameter has a critical exponent of $\beta=0.30\pm0.06$. (7) The integrated intensity of the diffuse ridge at the off-Bragg point $I((101))$ increases divergently immediately below T_m, and has a constant value at $T_G>T_m+5$ °C where 2D fluctuations are dominant. (8) The physical quantities mentioned above show no thermal hysteresis at T_m.

All the features except for (5) are strong evidence that the melting is characteristic of the second-order transition. On the other hand the feature (5) suggests that the transition has a very small but finite gap of the first-order transition. We conclude that the melting at the high P_{Rb} case is first order with a hardly appreciable gap.

(f) From the observed 2D nature of correlations at higher temperatures ($T_G>T_m+10$ °C), the interaction responsible for the transition is suggested to be 2D, but the observed critical exponent of order parameter and the ratio ξ_c/ξ_a indicate that the ordering around T_m is governed by the 3D interaction between such correlated 2D clusters.

(g) In the low-P_{Rb} case ($P_{\mathrm{Rb}}=6.1\times10$ Pa), $q_a((100))$ and $I((100))$ show a large discontinuity at T_m and the thermal hysteresis of about 0.2 °C, and any critical behaviors are hardly observed, which are characteristic of the first-order transition.

(h) The critical nature of the melting transition depends on P_{Rb}; the gap at T_m in order parameter decreases with increasing P_{Rb}, and appears to be zero for $P_{\mathrm{Rb}}\geq6.6\times10^3$ Pa. However in-plane and out-of-plane correlation lengths remain finite even for the highest P_{Rb} studied here.

(i) The structural phase transition from $\alpha\beta$ to $\alpha\beta\gamma\delta$ solid, which occurs at a temperature below T_m, accompanies a large discontinuous change in $I((100))$ and $q_a((100))$ and the thermal hysteresis of about 0.5 °C. This stacking transition is concluded at first order.

(j) The present melting transition is discussed in relation with the some theoretical works. The space group of the $\alpha\beta$ solid does not belong to any case of the second-order transition proposed for stage-1 alkali-metal GIC's in the calculations based on the Landau theory,[38,39] so that the observed discontinuity in ξ is consistent with the theoretical prediction. On the other hand the remarkable critical behavior characteristic of the second-order transition can be understood by the Monte Carlo calculation[41] for the 3D four-state Potts model in which nearly continuous change of the total energy E with a small gap at T_m and a sharp c_v peak are predicted.

ACKNOWLEDGMENTS

We gratefully acknowledge H. Aoki, S. Miyashita, Y. Murakami, and H. Zabel for stimulating and valuable discussions on the melting transition, and H. Asano for helpful suggestions on the phase diagram. We also thank T. Komatsubara for giving facilities of electron beam welder, and K. Suda, Y. Ito, T. Kishimoto, and H. Minemoto for offering technical advice.

[1]M. S. Dresselhaus and G. Dresselhaus, Adv. Phys. **30**, 139 (1981).

[2]*Intercalation in Layered Materials*, edited by M. S. Dresselhaus (Plenum, New York, 1986).

[3]S. A. Solin, Adv. Chem. Phys. **49**, 455 (1982).

[4]R. Nishitani, Y. Uno, and H. Suematsu, Phys. Rev. B **27**, 6572 (1983).

[5]M. E. Misenheimer and H. Zabel, Phys. Rev. Lett. **54**, 2521 (1985).

[6]P. A. Heiney, M. E. Huster, and V. B. Cajipe, Synth. Met. **12**, 21 (1985); M. E. Huster, P. A. Heiney, V. B. Cajipe, and J. E. Fischer, Phys. Rev. **B35**, 3311 (1987).

[7]G. Kirczenow, Phys. Rev. B **31**, 5376 (1985).

[8]S. A. Safran, Phys. Rev. Lett. **44**, 937 (1980).

[9]R. Clarke, J. N. Gray, H. Homma, and M. J. Winokur, Phys. Rev. Lett. **47**, 1407 (1981).

[10]H. Zabel, S. C. Moss, N. Caswell, and S. A. Solin, Phys. Rev. Lett. **43**, 2022 (1979).

[11]R. Nishitani, K. Suda, and H. Suematsu, J. Phys. Soc. Jpn. **55**, 1601 (1986).

[12]R. Clarke, N. Caswell, S. A. Solin, and P. M. Horn, Phys. Rev. Lett. **43**, 2018 (1979).
[13]M. J. Winokur and R. Clarke, Phys. Rev. Lett. **54**, 811 (1985).
[14]W. A. Kamitakahara and H. Zabel, Phys. Rev. B **32**, 7817 (1985).
[15]H. Zabel, S. E. Hardcastle, D. A. Neumann, M. Suzuki, and A. Magerl, Phys. Rev. Lett. **57**, 2041 (1986).
[16]A. Erbil, A. R. Kortan, R. J. Birgeneau, and M. S. Dresselhaus, Phys. Rev. B **28**, 6329 (1983).
[17]R. J. Birgeneau and P. M. Horn, Science **232**, 329 (1986).
[18]T. F. Rosenbaum, S. E. Nagler, P. M. Horn, and R. Clarke, Phys. Rev. Lett. **50**, 1791 (1983).
[19]*American Institute of Physics Handbook,* 2nd ed. (McGraw-Hill, New York, 1963).
[20]F. Rousseaux, R. Moret, D. Guerard, P. Lagrange, and M. Lelaurain, Synth. Met. **12**, 45 (1985).
[21]G. Reiter and S. C. Moss, Phys. Rev. B **33**, 7209 (1986).
[22]I. Naiki and Y. Yamada, J. Phys. Soc. Jpn. **51**, 257 (1982).
[23]Y. Yamada and I. Naiki, J. Phys. Soc. Jpn. **51**, 2174 (1982).
[24]M. Mori, S. C. Moss, Y. M. Jan, and H. Zabel, Phys. Rev. B **25**, 1287 (1982).
[25]M. Suzuki and H. Suematsu, J. Phys. Soc. Jpn. **52**, 2761 (1983).
[26]M. Suzuki, Phys. Rev. B **33**, 1386 (1986).
[27]R. Nishitani, Y. Uno, H. Suematsu, Y. Fujii, and T. Matsushita, Phys. Rev. Lett. **52**, 1504 (1984).
[28]H. Minemoto, Master's thesis, University of Tsukuba, 1985.
[29]H. Minemoto and H. Suematsu, Synth. Met. **12**, 33 (1985).
[30]W. D. Ellenson, D. Semmingsen, D. Guerard, D. G. Onn, and J. E. Fisher, Mater. Sci. Eng. **31**, 137 (1977).
[31]D. S. Robinson, Ph.D. thesis, University of Illinois, 1983; D. S. Robinson, T. C. McGlinn, J. L. Zarestky, and M. B. Salamon, *Graphite Intercalation Compounds, Extended Abstracts of the 1986 Fall Meeting of the Materials Research Society,* edited by M. S. Dresselhaus, G. Dresselhaus, and S. A. Solin (Materials Research Society, Pittsburgh, 1986).
[32]R. Clarke, N. Caswell, and S. A. Solin, Phys. Rev. Lett. **42**, 61 (1979).
[33]N. Caswell, Phys. Rev. B **22**, 6308 (1980).
[34]R. B. Potts, Proc. Cambridge Philos. Soc. **48**, 106 (1952).
[35]F. Y. Wu, Rev. Mod. Phys. **54**, 235 (1982).
[36]J. Rossat-Mignod, A. Wiedenmann, K. C. Woo, J. W. Millikeen, and J. E. Fisher, Solid State Commun. **44**, 1339 (1982).
[37]D. S. Robinson and M. B. Salamon, Phys. Rev. Lett. **48**, 156 (1982).
[38]P. Bak and E. Dommany, Phys. Rev. B **20**, 2818 (1979).
[39]C. R. Lee, H. Aoki, and H. Kamimura, J. Phys. Soc. Jpn. **49**, 870 (1980).
[40]H. Miyazaki, C. Horie, and T. Watanabe, J. Phys. Soc. Jpn. **53**, 3843 (1984).
[41]H. J. Hermmann, Z. Phys. B **35**, 171 (1979).
[42]Obtained from the fitting of the data in Ref. 19.
[43]*International Tables for X-Ray Crystallography,* edited by C. H. Macgillaury, G. D. Rieck, and K. Lonsdale (Kynoch, Birmingham, 1962), Vol. III.
[44]J. M. Ziman, *Principles of the Theory of Solids,* 2nd ed. (Cambridge University Press, Cambridge, England, 1972).
[45]F. J. Salzano and S. Aronson, J. Chem. Phys. **45**, 4551 (1966).
[46]P. Lagrange, D. Guerard, M. E. Makrini, and A. Herold, C.R. Acad. Sci. Paris, Ser. C **287**, 179 (1978).
[47]The small peaks at (201), (202), and (203) in Fig. 8, which do not fit the above rule ($l=4n$, n integer), may come from the mosaic spread effect. The line broadening of the Bragg peak at $l=0,4$ in the (20l) and (22l) scan is ascribed to the mosaic spread effect, but presumably not from the stacking fault because it is remarkable for a smaller l.
[48]H. Suematsu, K. Suda, and N. Metoki, Synth. Met. **23**, 7 (1988).
[49]Y. Chabre, P. Segransen, C. Berthier, F. J. Disalvo, and J. E. Fisher, Synth. Met. **8**, 7 (1983).
[50]F. J. Salzano and S. Aronson, J. Chem. Phys. **42**, 1323 (1965).
[51]F. J. Salzano and S. Aronson, J. Chem. Phys. **43**, 149 (1965).
[52]F. J. Salzano and S. Aronson, J. Chem. Phys. **44**, 4320 (1966).
[53]F. J. Salzano and S. Aronson, J. Chem. Phys. **45**, 2221 (1966).
[54]*Phase Transition and Critical Phenomena,* edited by C. Domb and M. S. Green (Academic, London, 1983), Vol. 3.
[55]In a more strict model we should take account of the $\alpha\beta$ stacking, which acts as an antiferromagnetic-like out-of-plane interaction.
[56]P. R. Nelson and B. I. Halperin, Phys. Rev. B **19**, 2457 (1979).
[57]A. P. Young, Phys. Rev. B **19**, 1855 (1979).
[58]J. M. Kosterlitz and D. J. Thouless, J. Phys. C **6**, 1181 (1973).
[59]H. Zabel (private communication).